Photo- and thermionic emission from potassium-intercalated carbon nanotube arrays

Tyler L. Westover,[a] Aaron D. Franklin, Baratunde A. Cola, Timothy S. Fisher,[b] and Ronald G. Reifenberger
Birck Nanotechnology Center, Purdue University, 1205 W. State St. West Lafayette, Indiana 47907

(Received 6 November 2009; accepted 22 February 2010; published 31 March 2010)

Carbon nanotubes (CNTs) are promising candidates to create new thermionic- and photoemission materials. Intercalation of CNTs with alkali metals, such as potassium, greatly reduces their work functions, and the low electron scattering rates of small-diameter CNTs offer the possibility of efficient photoemission. This work uses a Nd:YAG (YAG denotes yttrium aluminum garnet) laser to irradiate single- and multiwalled CNTs intercalated with potassium, and the resultant energy distributions of photo- and thermionic emitted electrons are measured using a hemispherical electron energy analyzer over a wide range of temperatures. For both single- and multiwalled CNTs intercalated with potassium, the authors observe a temperature dependent work function that has a minimum of approximately 2.0 eV at approximately 600 K. At temperatures above 600 K, the measured work function values increase with temperature presumably due to deintercalation of potassium atoms. Laser illumination causes the magnitudes of collected electron energy distributions to increase substantially but in many cases has little effect on their shape. Simple theoretical models are also developed that relate the photo- and thermionic emission processes and indicate that large numbers of photoexcited electrons partially thermalize (i.e., undergo one or more scattering events) before escaping from the emitter surface. © *2010 American Vacuum Society.*
[DOI: 10.1116/1.3368466]

I. INTRODUCTION

Because of their exceptional properties, carbon nanotubes (CNTs) represent a promising class of new thermionic- and photoemission materials. CNTs have very high mechanical strength and high-temperature stability and can be doped with different materials to alter their electronic and emission properties. The work function of pristine CNTs is similar to that of graphite ($\phi \approx 4-5$ eV) (Refs. 1–3) and can be reduced to 2–3 eV by the introduction of alkali metal intercalants.[4,5] Robinson *et al.*[6] showed that intercalated potassium metal atoms can be stable in graphitic nanofibers at temperatures of up to 970 K, indicating that emission from intercalated carbon nanostructures may exhibit greater long-term stability than that from planar emitting cathodes. Small diameter CNTs are particularly promising as photo-/thermionic emitters for several reasons. Quantum confinement in such structures forces electrons to occupy distinct energy quantum states and reduces electron scattering rates. Furthermore, CNTs are highly absorptive in the range of dominant solar wavelengths.[7,8]

Previous work[9] has demonstrated that intercalated potassium atoms can be stable in CNTs at temperatures as high as 820 K and, consequently, may be useful in applications such thermionic emission power generators[10–13] and electron accelerators.[14–16] Thermionic energy conversion requires operating temperatures in the range of 600–750 K for useful levels of power generation and efficiency.[10–12] Thus, the high-temperature stability of alkali metal intercalants in carbon-based nanostructures is crucial in thermionic energy converters. For accelerator applications, field emission electron sources provide the highest current densities and smallest beam emittances; however, their implementation is plagued with technical challenges, such as maintaining ultrahigh vacuum and preventing electron emission from microscopic cracks or impurities on the chamber walls.[14,17,18] Consequently, thermionic and thermally assisted photoemission sources are still preferred for generating electrons for most accelerator applications.[14,15,19] Therefore, the temperature response of alkali metal intercalants in carbon-based nanostructures is important in electron emission applications.

In this work, we irradiate potassium-intercalated single-walled CNTs (SWCNTs) and multiwalled CNTs (MWCNTs) with a 100 mW Nd:YAG (YAG denotes yttrium aluminum garnet) laser (532 nm) and measure the resultant energy distributions of photoemitted and thermionic electrons using a hemispherical electron energy analyzer. We observe that irradiating potassium-intercalated CNT arrays with 532 nm laser illumination substantially increases the electron emission intensity above that which is obtained from thermionic emission alone. In addition, this work provides insights into the energy transport processes involved in photo-/thermionic electron emission, such as absorption of the incident radiation and scattering of the excited electrons, and provides some insights toward increasing electron emission and efficiency of CNT-based thermionic- and photoemission materials.

The organization of this article is as follows. First, simplified thermionic- and photoemission theories are briefly

[a]Electronic addresses: tyler.westover@gmail.com and twestov@sandia.gov
[b]Author to whom correspondence should be addressed; electronic mail: tsfisher@purdue.edu

outlined. The next sections describe the intercalation process and the experimental setup, and the last section contains experimental results from three samples. The first sample is single-crystal tungsten (100) used to calibrate the energy analyzer, and the last two samples are, respectively, single- and multiwalled CNT samples intercalated with potassium. Finally, we present our conclusions.

II. THEORETICAL MODELS

A. Thermionic emission

Although the theory of thermionic emission is well developed, we briefly visit the topic here to cast it in a form that is most suitable for comparison to photoemission. We begin with the energy distribution of electrons thermionically emitted from a free-electron material,[20,21]

$$I_{\text{therm}}(E)dE = \frac{4\pi m}{h^3}\frac{(E - E_F - \phi)}{1 + \exp(E - E_F/k_BT)}H(E - E_F - \phi)dE, \tag{1}$$

where $I_{\text{therm}}(E)$ is the intensity of thermionic electrons at a specified energy E, m is the electron rest mass, h is Planck's constant, k_B is Boltzmann's constant, ϕ is the material's work function, and E_F is the emitter's Fermi level. In order to arrive at the simple form of Eq. (1), it is assumed that all electrons with energies greater than the surface barrier height $E_F+\phi$ successfully escape from the emitter, and that electrons with less energy cannot (i.e., quantum tunneling has been neglected because the vacuum barrier is much thicker than the electronic wavelength). This assumption, known as the Richardson approximation, is represented in Eq. (1) by the Heaviside step function $H(E-E_F-\phi)$. The thermionic emission energy distribution (EED) predicted by Eq. (1) is sharply peaked with a maximum at $E=E_F+\phi+k_BT$, and thus, by comparing the theoretical energy distribution with that obtained from experiments, Eq. (1) can be conveniently used to estimate the work function of a material.

The thermionic emission saturation current density J_{therm} is obtained by integrating Eq. (1) over all energies and multiplying by the electron charge e,

$$J_{\text{therm}} = e\int_0^\infty I_{\text{therm}}(E)dE = \frac{4\pi me}{h^3}(k_BT)^2\left[\frac{\pi^2}{6} + \frac{1}{2}\left(\frac{\phi}{k_BT}\right)^2 + \text{dilog}\left(1 + \frac{\phi}{k_BT}\right)\right], \tag{2}$$

where dilog( ) is the dilogarithm function, which can be efficiently calculated as a series[22,23] (also see the Appendix). We note that the form given in Eq. (2) is especially well suited for comparing J_{therm} with the current density of photoemitted electrons J_{phot}, which is the topic of Sec. II B. With the additional assumption that the material work function ϕ is much greater than k_BT (ϕ is approximately 2–5 eV, while k_BT is 0.03 eV at 300 K), Eq. (2) can be simplified to the widely known Richardson–Laue–Dushman equation,

$$J_{\text{therm}} = A^*T^2\exp\left(\frac{-\phi}{k_BT}\right), \tag{3}$$

where A^* represents the apparent emission constant and is equal to 120 A cm^{-2} K^{-2} for an ideal, metallic emitter.[24]

Importantly, the above formulation assumes that the emitter is a free-electron material with a single parabolic conduction band that can be characterized with an effective mass approximation. The free-electron assumption is valid for materials in which the conduction band is easily populated, such as metals, some semiconductors, and some semimetals (including graphite). Prior works on nanocrystalline diamond,[25,26] boron-doped nanocrystalline diamond films,[11] and potassium-intercalated carbon nanofibers[6] have employed the free electron and effective mass approximations to obtain good agreement between measured emission energy distributions and theoretical curves. The results presented below show that the same approximations are applicable to thermionic and photoemission from potassium-intercalated carbon nanotubes (K/CNTs).

B. Photoemission

Photoemission (i.e., emission of electrons by photoexcitation via the photoelectric effect) is inherently a quantum mechanical phenomenon that depends on emitter geometry and electronic band structure. Highly sophisticated photoemission models[27,28] have been developed that treat the quantum mechanical coupling between the initial and the final energy states occupied by electrons before and after photoexcitation. However, these simulations are primarily intended for ideal emitters with planar surfaces and simple electronic band structures, and it is not yet clear how they apply to nanostructured materials because coupling of electromagnetic fields with electrons in nanoemitters is not straightforward. The present work explores photoemission from CNT arrays intercalated with potassium atoms, where neither the geometry nor the band structure is precisely known. Consequently, a simpler approach is employed to interpret photoemission from such structures.

Recently, Jensen *et al.*[19] introduced an adaptation of the basic Fowler–DuBridge photoemission model[29,30] and demonstrated good agreement between predictions and experimental data obtained from a needle-shaped scandate dispenser photocathode. The Fowler–DuBridge photoemission model, which was developed in the 1930s, has also successfully predicted photoemission from other materials.[31,32] In the present work, we employ a slightly different adaptation of the Fowler–DuBridge model that incorporates three significant modifications. First, the present formulation emphasizes the similarity between photoemission and thermionic emission; second, it avoids the necessity of using different calculations for cases in which the photon energy is greater than or less than the emitter's work function; and third, the present formulation does not rely on extensive integration approximations that in some situations compromise the pre-

cision of results. The present formulation is, however, still limited by the simple nature of the photoemission model itself.

In the Fowler–DuBridge model,[29,30] the number of photoemitted electrons is evaluated as the product of the several factors to account for laser intensity, light absorptance (spectral directional absorptance), and the fraction of absorbed photons that potentially contribute to electron emission. Several assumptions are invoked. First, all electrons in the emitter's conduction band are assumed to have an equal probability of absorbing photons and, consequently, photon absorption is dominated by low energy electrons as prescribed by the Fermi–Dirac electron distribution function. Second, the quantum transmission function is estimated using the Richardson approximation described above in which the probability of emission is unity for electrons with normal energy greater than the surface barrier and is zero for all others. Third, it is assumed that all of the energy that electrons acquire from photoexcitation is converted into kinetic energy in the direction perpendicular to the surface, which is the optimal condition for emission. Admittedly, the last assumption is overly optimistic; however, when the photon energy $\hbar\omega$ is approximately equal to or less than the work function ϕ, the majority of electrons that surpass the barrier and emit into vacuum will have necessarily scattered in a direction nearly perpendicular to the surface upon absorbing a photon. Further, in this work, we normalize the experimental data and model predictions such that the comparisons focus on the shape of the energy distributions and not on the differences in the magnitude of the emitted flux. The effect of the third assumption on the shapes of predicted energy distributions of photoemitted electrons is revisited below.

Analogous to Fowler,[29] we define the number of available electrons N_{avail} as the number of electrons that reach the emitter surface per second per unit area and that can potentially escape into vacuum via photoexcitation (i.e., that have sufficient normal kinetic energy W to overcome the surface barrier if W is augmented by a photon of energy $\hbar\omega$). Thus, the fraction of absorbed photons that potentially causes photoemission is given by $N_{\text{avail}}/N_{\text{tot}}$, where N_{tot} is the total number of conduction-band electrons that arrive at emitter surface per second per unit area. The number of available electrons N_{avail} is most easily obtained by integrating the total energy distribution of photoemitted electrons $I_{\text{phot}}(E)$. Within the framework of the simple photoemission model described above, $I_{\text{phot}}(E)$ is found by simply shifting the energy E in the Fermi–Dirac function of Eq. (1) (the denominator) by the photon energy $\hbar\omega$,

$$I_{\text{phot}}(E)dE = \frac{4\pi m}{h^3}\frac{(E - E_F - \phi)}{1 + \exp\left(E - E_F - \hbar\omega/k_BT\right)} \times H(E - E_F - \phi)dE. \tag{4}$$

The number of available electrons is obtained from Eq. (4) by integrating over all electron energies as performed above for the thermionic emission current density,[33]

$$N_{\text{avail}} = \int_0^\infty I_{\text{therm}}(E)dE = \frac{4\pi m}{h^3}(k_BT)^2\left[\frac{\pi^2}{6} + \frac{1}{2}\left(\frac{\phi - \hbar\omega}{k_BT}\right)^2 + \text{dilog}\left(1 + \frac{\phi - \hbar\omega}{k_BT}\right)\right]. \tag{5}$$

The arrival rate of all conduction-band electrons at the emitter surface per unit area N_{tot} is well approximated at finite temperatures by its value at absolute zero because the energy distribution of electrons within materials is only a weak function of temperature. Consequently, for a free electron material with a single conduction band N_{tot} is[34]

$$N_{\text{tot}} = \frac{2\pi m}{h^3}E_F^2, \tag{6}$$

where E_F is measured from the bottom of the conduction band. Invoking the assumptions discussed above and with N_{avail} and N_{tot} defined by Eqs. (5) and (6), the electron emission current density due to photoexcitation is approximated as

$$J_{\text{phot}} = 2e\alpha_{\text{abs}}\frac{I_{\text{laser}}}{\hbar\omega}\left(\frac{k_BT}{E_F}\right)^2\left[\frac{\pi^2}{6} + \frac{1}{2}\left(\frac{\phi - \hbar\omega}{k_BT}\right)^2 + \text{dilog}\left(1 + \frac{\phi - \hbar\omega}{k_BT}\right)\right], \tag{7}$$

where α_{abs} is the optical absorptance of the emitter at the wavelength of illumination and I_{laser} is the intensity of laser illumination (W/cm^2). Comparison of Eqs. (2) and (7) reveals that the effects of temperature T and work function ϕ on photoemission and thermionic emission are similar except that the emitter's work function ϕ in Eq. (2) is replaced by $\phi - \hbar\omega$ in Eq. (7). We emphasize that the photoemission current density J_{phot} predicted by Eq. (7) is based on the arrival rate of electrons at the emitter surface rather than on the electron concentration per unit of emitter volume. Consequently, J_{phot} derived here is slightly different than that of the basic Fowler–DuBridge model. In fact, J_{phot} derived here is equivalent to J_{phot} of the Fowler–DuBridge model multiplied by the ratio $\bar{v}_{x,\text{avail}}/\bar{v}_{x,\text{tot}}$, where $\bar{v}_{x,\text{avail}}$ and $\bar{v}_{x,\text{tot}}$ are the mean values of the x-component of velocity of the electrons included in N_{avail} and N_{tot}, respectively. However, $\bar{v}_{x,\text{avail}}$ is approximately equal to $\bar{v}_{x,\text{tot}}$ so that the value of J_{phot} derived here is in good agreement with that obtained from the basic Fowler–DuBridge model. For example, as shown in Ref. 9, predictions of Eq. (7) are in good agreement with those of Eq. (14) in Ref. 19.

It is instructive to compare the predicted energy distributions of thermionic and photoemitted electrons, and representative normalized curves are shown in Fig. 1 for a photon energy $\hbar\omega$ of 2.33 eV ($\lambda = 532$ nm) and emitter work functions of 1.8, 2.1, and 2.4 eV. For comparison, Fig. 1 also includes predicted EEDs assuming that the photon energy $\hbar\omega$ has an equal probability of being absorbed as kinetic energy in *any* direction (instead of being confined to only the direction normal to the emitter surface). The necessary calculations have already been described[9] and the resulting ex-

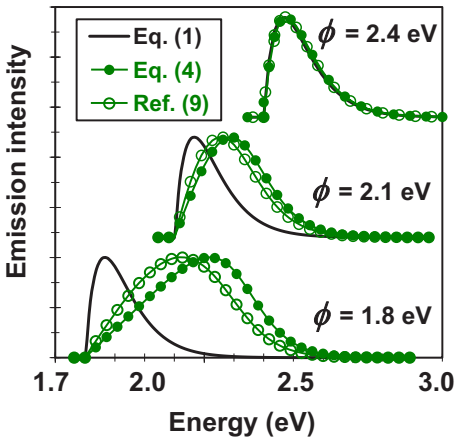

FIG. 1. (Color online) Predicted electron EEDs for pure thermionic emission [Eq. (1)] and for two simple photoemission models. One photoemission model [Eq. (4)] assumes that all of the photon energy $\hbar\omega$ is converted into "normal energy" while the other photoemission model (Ref. 9) assumes that $\hbar\omega$ has an equal probability of being absorbed as kinetic energy in any direction. All curves are normalized to facilitate comparison: $\hbar\omega$=2.33 eV and T=500 K.

pressions have been evaluated numerically. When the work function ϕ is greater than the photon energy $\hbar\omega$, all three emission models predict nearly identical EEDs. Significantly, however, as ϕ decreases below $\hbar\omega$, the photoemission energy distributions shift to higher energies because photoexcitation provides more energy than is needed to overcome the vacuum emission barrier. Figure 1 demonstrates that this effect is greatest for the modified Fowler–DuBridge model, which assumes that all of the photon energy $\hbar\omega$ is converted into "normal energy" and is slightly mitigated when $\hbar\omega$ is assumed to contribute to electron kinetic energy in all directions with equal probability.

Although the energy distribution predicted by Eq. (4) is based on a very simple photoexcitation model and neglects electron scattering within the emitter, previous work has shown that it can yield good agreement with experimental data for some emitters. For example, Mogren and Reifenberger[35] used a similar model to create theoretical curve fits that closely matched threshold photoemission data from lanthum hexaboride, $LaB_6(100)$. However, Eq. (4) is not expected to be accurate for emitters in which quantum confinement affects the electronic density of states or in situations in which emitting electrons originate from the valence as well as the conduction band.[36] The results presented below show that the same approximations are applicable to thermionic and photoemission from potassium-intercalated carbon nanotubes (K/CNTs).

C. Laser heating of substrate

Experimental evidence presented below demonstrates that laser heating of the substrate is small. Nevertheless, because both thermionic and photoemission of electrons depend strongly on temperature, a thermal model of the substrate is desirable. The emphasis of the development here is to place an upper bound on the temperature rise in the substrate due to laser heating and to show that this upper bound is consistent with experimental results presented below. Assuming that the laser beam and substrate are axisymmetric, the equation governing the local temperature rise in the substrate ΔT_{sub} is two dimensional and has the form

$$\frac{1}{r}\frac{d}{\partial r}\left(r\frac{d\Delta T_{sub}}{\partial r}\right)+\frac{d^2\Delta T_{sub}}{\partial z^2}=0, \tag{8}$$

where r and z are the radial and vertical coordinates, respectively. Heat flux through the top surface of the sample is approximated as a constant value of q''_0 for $r<d_0/2$ and is assumed to be 0 for $r>d_0/2$, where d_0 is the approximate diameter of the laser beam. To place an upper bound on ΔT_{sub}, the lower boundary of the substrate is assumed to be adiabatic and the temperature rise at the outer radial boundary is assumed to be zero. The latter boundary condition is justified because experiments have proven that laser illumination does not heat a substantial portion of the substrate.[37] With the boundary conditions outlined above, the local temperature rise in the sample can be expressed as[38]

$$\Delta T_{sub}(r,z)=\sum_{n=1}^{\infty}\frac{q''_0 d_0 J_1(\Lambda_n r/r_{sub})\sinh(\Lambda_n Z/r_{sub})J_0(\Lambda_n r/r_{sub})}{k_{sub}\Lambda_n^2\cosh(\Lambda_n t_{sub}/r_{sub})[J_1(\Lambda_n)]^2}, \tag{9}$$

where r_{sub} is the substrate radius ($\approx$0.5 cm), t_{sub} is the substrate thickness (0.5 mm), and k_{sub} is the substrate thermal conductivity ($\approx$150 W/cm^2 at 300 K). J_0 and J_1 are Bessel functions of the first kind of order zero and one, respectively, and Λ_n are the sequential zeros of J_0 [given by 2.404, 5.520, 8.653,… (see Ref. 38)]. Laser intensity q''_0 is assumed to be 320 W/cm^2, which corresponds to a 100 mW beam focused to 0.2 mm. Substituting numerical values for the parameters in Eq. (9) yields a maximum estimated temperature rise of approximately 2 K at the center of the laser beam. Thus, theoretical considerations indicate that laser heating is a small effect.

D. Energy convolution

The electron EEDs reported here were measured using a hemispherical energy analyzer. In the measurement process, the EED is convolved with a Gaussian spreading function due to interaction with the energy analyzer apparatus. Correct interpretation of experimental data requires accounting for effects of the spreading function, which depends on the specific analyzer settings and takes the form[39,40]

$$G_1=\frac{1}{\sigma\sqrt{2\pi}}\exp\left[-\frac{1}{2}\left(\frac{E-E'}{\sigma}\right)^2\right]. \tag{10}$$

The effects of the analyzer settings are manifest in the standard deviation σ, which is commonly referred to as "analyzer resolution. EEDs obtained from the analyzer are convolutions of Eq. (10) with Eq. (2) or Eq. (4), for thermionic or photoemission, respectively. For small values of σ, the distributions given by Eqs. (2) and (4) are affected very little, allowing for accurate estimates of emitter work function ϕ.

However, as the analyzer resolution σ increases, the convolution of Eq. (10) with Eq. (2) or Eq. (4) smears the energy peak, and the estimates of emitter work function ϕ become less accurate. The work function of the electron detector is another important parameter and must be known in order to properly position measured EEDs on the energy axis. The analyzer resolution σ and the work function of the electron detector are determined by calibrating the electron analyzer using a free-electron material with a known work function, as described in Sec. III.

In practice, the work function of many surfaces is not uniform but instead depends on local surface conditions, such as crystallographic orientation and the presence of impurities or adsorbates. If a surface consists of a few areas with distinct work function values, then the thermionic energy distribution can contain multiple peaks whose relative intensities depend on the effective area and work function of each emission site.[11] Samples that have a moderate work function variation across their surface may exhibit broadening of the EED, although only a single peak may be distinguishable. Variation in the work function along a sample surface can also create strong lateral electric fields parallel to the surface that causes the surface to exhibit a single apparent work function value.[41,42]

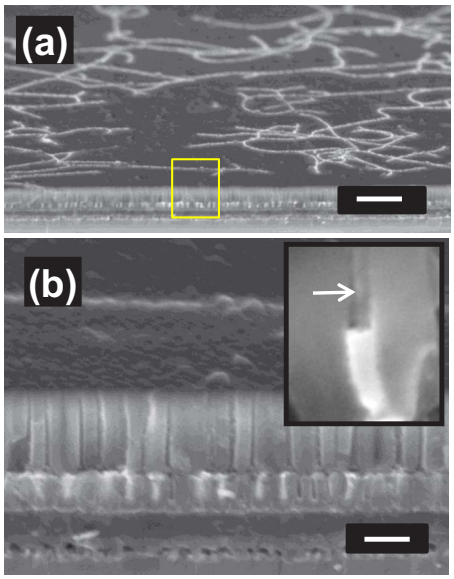

FIG. 2. (Color online) (a) Tilted cross-sectional FESEM showing the PAA surface with SWCNTs extending from pores. (b) FESEM of the area in the yellow box in (a). White material in the bottom of the pores is palladium and provides electrical contact to the SWCNTs. The inset shows a Pd-contacted SWCNT in a PAA pore. Scale bar is 1 μm in (a) and 200 nm in (b).

III. EXPERIMENTAL AND SIMULATION RESULTS

A. Sample preparation

EEDs of thermionic and photoexcited electrons were collected from several potassium-intercalated single-walled and multiwalled carbon nanotubes. Vertical SWCNTs were grown by microwave-plasma-enhanced chemical vapor deposition (MPECVD) in porous anodic alumina (PAA) using processes that have been described elsewhere.[43–45] Figure 2 contains field emission scanning electron microscope (FESEM) images of typical SWCNTs grown in PAA before loading with potassium metal atoms. A complete description of the SWCNT/PAA structure and additional FESEM images are available.[43–45] Multiwalled CNTs were also grown using MPECVD on silicon wafers, and details of the process can be found in Ref. 46.

The process by which all of the samples were intercalated with potassium atoms consisted of depositing a layer of potassium (estimated depth of 30–60 nm) on the sample surface, and then heating the sample to an appropriate temperature corresponding to a stage-1 (C_8K) or stage-2 ($C_{24}K$) K/CNT intercalate.[47,48] We note that for the case of graphite, the stage number refers to the number of carbon planes between each potassium layer. Consequently, speaking of intercalation of single-walled structures, such as individual SWCNTS, is not strictly correct. For such structures, loading with foreign atoms, such as potassium, may be referred to as encapsulation.[5] However, to avoid otherwise cumbersome expressions, we use the term "intercalation" to denote loading of MWCNTs and SWCNTs with potassium.

For control experiments, the same intercalation procedure was also performed on bare silicon wafers and bare PAA structures without CNTs. The details of the reaction procedure are described below. Potassium (Alpha Aesar, 5 g bars, 99%, stored in mineral oil) is intercalated into the carbon nanotubes using an adaptation of a method reported earlier.[47] After rinsing the as-grown carbon nanotube sample in acetone and methanol to remove contaminants, the sample is placed in a custom-made Pyrex-Kovar reaction vessel that is capped with a VCR fitting rated to hold high-vacuum up to 700 K. The reaction vessel is then introduced to an argon atmosphere in a glovebox (O_2 and H_2O content <1 ppm). Inside the glovebox, potassium bars are cleaned with petrol ether to remove the mineral oil, and oxidized faces are removed with a knife. Then, approximately 1 g of potassium is placed in the reaction vessel immediately adjacent to the sample.

An inert atmosphere is necessary to accomplish this task because potassium metal readily reacts with oxygen in ambient air, forming oxides that can impede intercalation of potassium atoms into the carbon lattice. Even in the high-purity argon atmosphere of the glove box, oxidation of potassium is noticeable, as evidenced by the fact that the shiny appearance of freshly cut potassium surfaces turns somewhat dull within a few minutes. To minimize oxidation of the potassium source during the intercalation process, the reaction vessel is sealed immediately after the potassium is placed inside.

The Pyrex/Kovar vessel is then removed from the glovebox and heated to approximately 540 K for a period of 2 days. At this temperature, the potassium (melting temperature of 337 K) inside the reaction vessel assumes a liquid form with an accompanying vapor that slowly deposits potassium atoms on the sample surface and on the glass walls of the reaction vessel. The thickness of the deposited potas-

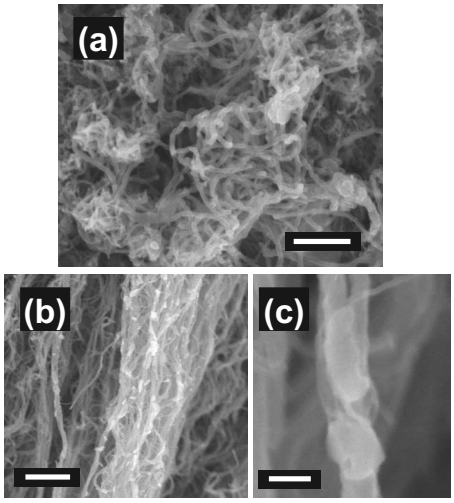

FIG. 3. FESEM images of K/MWCNTs, showing metal, presumably potassium, inside individual MWCNTs. Scale bars are 500 nm, 1 μm, and 100 nm, in (a), (b), and (c), respectively.

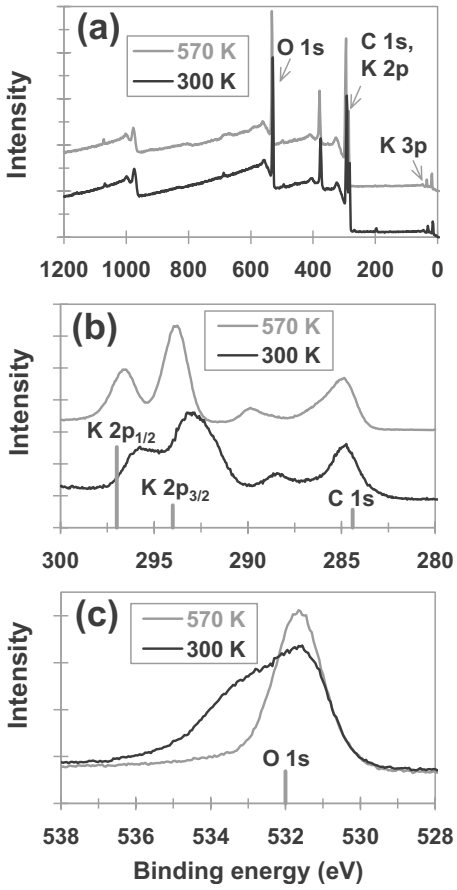

FIG. 4. X-ray photoemission intensity of a K/MWCNT sample as a function of binding energy at temperatures of 300 and 570 K. XPS data were obtained by Zemlyanov of the Surface Analysis Laboratory, Birck Nanotechnology Center, Purdue University.

sium layer is estimated by the transparency of the glass walls of the reaction vessel. Initially, the glass is transparent. After the deposition process, however, the glass is nearly opaque, indicating a potassium depth of 30–60 nm. We expect that the depth of the potassium layer on the surface of the sample is approximately the same as that on the glass because potassium's sticking coefficient is approximately the same for both surfaces after a few monolayers of potassium have been deposited, causing both surfaces to behave as elemental potassium. The final step of the potassium intercalation process consists of reheating the sample to approximately 340 K and maintaining that temperature for approximately 12 h. After completion of the intercalation process, bulk potassium in the reaction vessel exhibits a silvery shine characteristic of pure potassium, indicating that an inert atmosphere is maintained throughout the entire procedure. In addition, small, shiny spots of potassium are often observed to decorate the sample surface. Presumably these potassium dots correspond to nucleation sites where large numbers of vaporized potassium atoms solidify on the sample surface. Figure 3 displays FESEM images of MWCNTs after they were subjected to the potassium intercalation process and shows that many of the CNTs contain metallic particles. These metallic particles are not present in CNT samples before potassium intercalation, leading us to believe they are potassium.

Prior work has shown that direct reaction of carbon nanofibers with molten potassium metal at 340 K results in the formation of stage-1 potassium intercalates, while higher temperatures result in lower loading of potassium atoms within carbon lattices.[47] In these prior studies, powder XRD and micro-Raman spectroscopy were used to confirm the formation of stage-1 potassium intercalate.[47,49] Additional studies have shown that stage-1 and stage-2 doping can also be achieved by depositing potassium atoms on CNTs at room temperature, although several days may be required for the alkali metal atoms to diffuse into the carbon lattice.[48] In the present study, potassium intercalation of a multiwalled CNT (K/MWCNT) sample was confirmed by x-ray photoelectron spectroscopy (XPS); unfortunately, potassium intercalation of single-walled CNTs grown in PAA (K/SWCNT/PAA) is not possible because the density of the SWCNTs within the PAA structure is too low for accurate XPS characterization.

XPS results obtained from a K/MWCNT sample at 300 and 570 K are shown in Fig. 4. The full energy spectrum results of Fig. 4(a) are dominated by carbon, potassium, and oxygen. Figure 4(b) focuses on the energy range of 280–300 eV. The peaks centered at 296.9 and 294.1 eV are attributed to K $2p_{1/2}$ and K $2p_{3/2}$, respectively, because they are approximately 2.8 eV apart and the ratio of their intensities is approximately 2.[50,51] The shift of the K $2p$ peaks to lower energies at a temperature of 300 K is caused by the presence of potassium oxides, which have a lower binding energy than pure K metal.[50,51] Thus, it appears that more K metal is present at 570 K than at 300 K, which is consistent with Ref. 5 wherein valence band photoemission spectra was used to show that potassium oxides on K-intercalated SWCNTs could be completely eliminated by annealing in vacuum at 877 K. However, even at this temperature, K atoms remained encapsulated within the SWCNTs.[5]

We note that the observed shifting of the K $2p_{1/2}$ and K $2p_{3/2}$ binding energies with temperature is real and not an

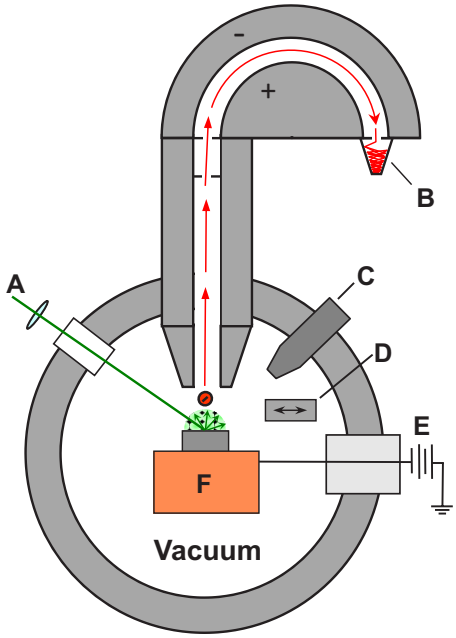

FIG. 5. (Color online) Schematic of hemispherical energy analyzer and vacuum system used to measure energy distributions of emission electrons. Labels have the following meanings: (a) incident laser, (b) electron multiplier, (c) pyrometer temperature probe, (d) movable metal plate, (e) direct-current voltage supply (V_{accel}), and (f) sample heater.

artifact of an extraneous effect such as surface charging because the C 1*s* peak at approximately 285 eV does not shift significantly with temperature. At 570 K, the C 1*s* peak is broadened and becomes asymmetrical with a tail on the high-energy side, which is also a characteristic of K-intercalated graphite, and confirms that K-intercalation is actually higher at 570 K than at 300 K. More exact specification of the K concentration is difficult because the CNT and K concentrations are not necessarily uniform over the entire sample surface. It is known that K atoms penetrate the walls of some CNTs much more readily than others.[48] Based on SEM images such as the one in Fig. 3, we believe that relatively few of the total number of CNTs are actually intercalated with K atoms.

Lastly, the XPS spectra in the region of the O 1*s* state are shown in Fig. 4(c). The O 1*s* peak at 300 K is much wider than that at 570 K, and the broadening at low temperature is likely due to greater amounts of potassium oxides which are known to cause spreading of the O 1*s* line.[52] Peaks in XPS spectra in the range 527–537 eV have been reported for K_2O.[52] Additional peaks have also been observed for K_2O_2, K_2O_3, and KO_2 at 531, 532, and 534.2 eV, respectively.[52]

B. Experimental setup

A SPECS-Phoibos 100 SCD hemispherical energy analyzer was used to measure the EEDs presented in this work. The emitter sample was heated using a molybdenum stage (HeatWave Laboratories, Inc.) and was located at the analyzer's focal plane 40 mm below the analyzer's aperture as shown in Fig. 5. A K-type thermocouple embedded 1 mm below the heater surface monitored the heater temperature,

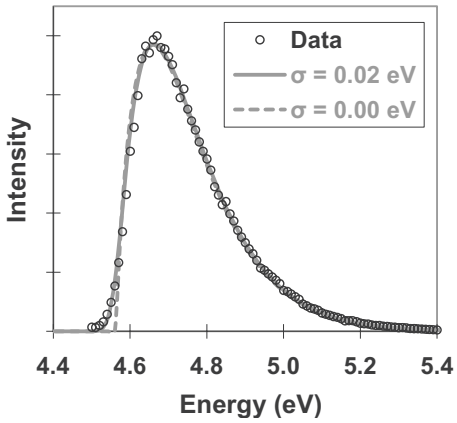

FIG. 6. Normalized EED data from single-crystal tungsten (100) at approximately 1140 K. The work function of tungsten (100) is known to be approximately 4.56 eV, indicating that the analyzer's work function is 3.98 eV.

which was maintained using a PID-controlled (PID denotes proportional-integral-derivative) power supply. Measurements of the sample's surface temperature were also available from an optical pyrometer, which was installed opposite the laser. With the laser shuttered, temperature measurements obtained from the pyrometer were within 30 K of those registered by the thermocouple. Alumina spacers were used to isolate the heater assembly thermally and electrically from other components in the vacuum chamber, and a small negative bias V_{accel} was applied to the heater surface to accelerate emitted electrons across the vacuum region and into the analyzer, whose detector has a work function of 3.98 eV. The negative bias was supplied by a Hewlett Packard 6542A dc power supply equipped with voltage sense lines that reduce uncertainty in the acceleration voltage to ± 0.003 V. A 100 mW Nd:YAG laser (532 nm) illuminated the sample through a 3.2 cm diameter view port positioned 45° above the horizon as viewed from the sample. A moveable metal plate located above the sample could be positioned to intercept specular reflection of the laser beam from the sample surface, although visual inspections indicated that laser reflection from most CNT samples was predominantly diffuse. The entire system was situated within a vacuum chamber evacuated to approximately 5×10^{-8} Torr.

C. Tungsten (100) calibration

Figure 6 shows a normalized EED obtained from a tungsten (100) sample (Matek, Inc.) at approximately 1140 K. The steep increase in intensity near the sample work function ϕ is due to the sharp increase of the quantum transmission coefficient, which increases from zero for energies slightly less than ϕ to unity for energies substantially greater than ϕ [this effect is approximated by the step function in Eq. (1)]. The gently sloping high-energy tail is a result of the partial occupation of high-energy states within the emitter according to Fermi–Dirac statistics. Figure 6 also contains a least-squares fit obtained from the convolution of Eqs. (1) and (10). From the curve fit, the analyzer's work function was determined to be 3.98 eV. The instrument resolution σ was

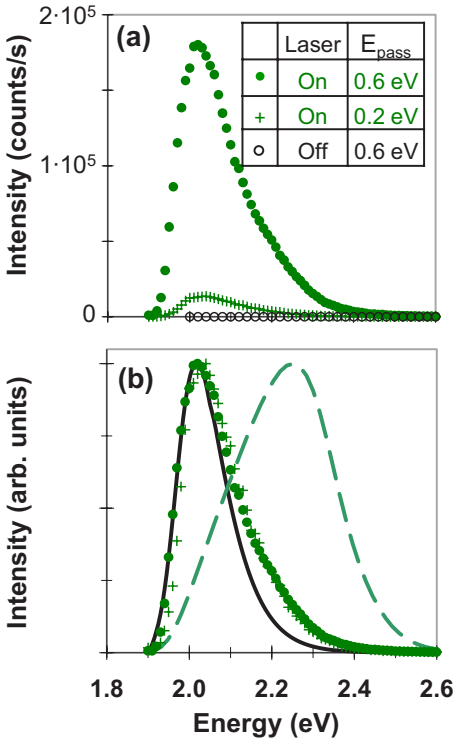

FIG. 7. (Color online) (a) EEDs from a K/SWCNT/PAA sample showing effects of electron pass energy E_{pass} and laser illumination. (b) Normalized data curves from (a). Data with laser shuttered are not shown in (b) because they are dominated by noise. Theoretical EEDs based on thermionic emission [Eq. (1), solid line] and photoemission [Eq. (4), dashed line] assuming ϕ=1.96 eV are included in (b) for comparison: T=570 K and V_{accel}=−4.5 V.

found to be 0.02 eV for the particular settings of the energy analyzer used in the measurement. The dashed gray line corresponds to Eq. (1) (σ=0 eV) and illustrates that broadening of the EED due to interactions of the emitted electrons with the energy analyzer apparatus is quite small for instrument resolution values of 0.02 eV and smaller.

D. K/SWCNT/PAA sample

Several samples containing regions with PAA, some with SWCNTs and some without, were subjected to the potassium-intercalation process described above. Results from a single representative K/SWCNT/PAA sample are shown below. Spectra from other samples manifested similar shapes with emission profiles of some samples being slightly narrower and those of others being slightly wider. Control samples without SWCNTs did not exhibit significant emission for temperatures below 600 K, indicating that CNTs are an essential component of the emission process. This observation is further substantiated below.

Because of the strong dependence of the emission intensity on temperature and illumination, it was necessary to adjust the analyzer's settings to keep the emission intensity in a range suitable for data acquisition. Figure 7, which contains representative EEDs collected at 570 K, explores the effects of laser illumination and electron pass energy E_{pass} (the kinetic energy of electrons that are collected by the detector) on the measured emission intensity. In Fig. 7(a) the curve traced by solid circles was collected with the pass energy E_{pass} set to 0.6 eV and the laser on. Shuttering the laser beam and leaving all other parameters unchanged resulted in spectra with practically negligible intensity (background noise).

The emission intensity with the laser on [solid circles in Fig. 7(a)] is sufficiently large that flooding of the electron detector could distort the shape of the measured energy distribution. To verify that this did not occur, another data set, denoted by small crosses, was recorded with the pass energy E_{pass} set to 0.2 eV. The analyzer's documentation indicates that measured emission intensity scales approximately as $(E_{pass})^n$ with n equal to 2.[53] Figure 7(b) shows normalized data recorded while the laser illuminated the sample and demonstrates that adjusting the pass energy E_{pass} had little effect on the shape of the distribution. However, as shown in Fig. 7(a), adjusting E_{pass} dramatically affected the magnitude of the measured energy distribution. Specifically, reducing E_{pass} from 0.6 to 0.2 caused the peak value (maximum intensity) of the measured energy distribution to drop from 1.80×10^5 counts/s to 1.36×10^4 counts/s (i.e., reducing E_{pass} by a factor of three caused the emission intensity to decrease by a factor of 13.2), which corresponds to a value for n of approximately 2.35, in good agreement with expectation. We also note that many other factors, such as analyzer acceptance angle, experimental geometry, and electric bias applied to the heater stage, can affect the shapes of measured EEDs. Consequently, additional experiments have been conducted to verify that the shapes of recorded EEDs are independent of reasonable changes in the experimental parameters. For example, the heater stage position and electric bias (electron acceleration bias) have negligible effect on our results over ranges of at least 5 mm in all directions and 3 V, respectively.

Theoretical curve fits based on thermionic theory [Eq. (1), solid line] and the simple photoemission theory outlined above [Eq. (4), dashed line] are also shown in Fig. 7(b) for comparison. Surprisingly, the photoexcited EED data follow thermionic theory much more closely than they do simple photoemission theory. One explanation for this unexpected behavior is that a large portion of photoexcited electrons partially thermalize (i.e., undergo one or more scattering events) before escaping from the sample, and this possibility is explored further below. Another possibility is that the laser enhancement manifest in the measured EEDs of Fig. 7 is not due directly to electron photoexcitation but instead is caused by laser heating of the substrate, and this concern is addressed in Fig. 8, which shows the effects of temperature. After the data in Fig. 7 was recorded, the K/SWCNT/PAA sample was cooled to room temperature and then additional spectra, shown in Fig. 8(a), was sequentially recorded as the sample was reheated to 570 K. Each of the EEDs were recorded after sufficient time had passed at each temperature to allow transient effects to subside, and the results include both dark conditions as well as those for illumination from a 532 nm, 100 mW unfocused laser (intensity ≈50 W/cm^2 over a spot with a diameter of approximately 0.5 mm). The location of the laser beam on the sample was adjusted to maximize

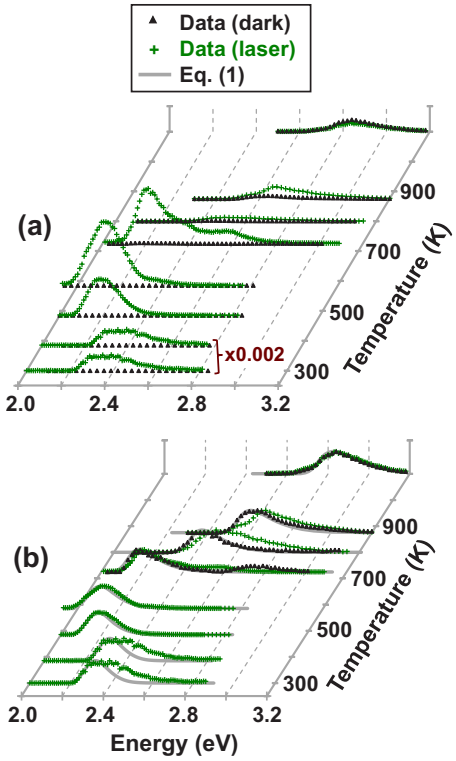

FIG. 8. (Color online) Thermionic and laser-assisted EEDs from the same K/SWCNT/PAA sample featured in Fig. 7. In (a) the EED magnitudes have been adjusted to account for the energy analyzer's settings and in (b) the EEDs have been normalized and theoretical fits based on Eq. (1) have been included. Data in (a) dominated by background noise are not shown in (b); $V_{accel}=-4.5$ V.

the emission signal, and all data shown were obtained with the laser beam illuminating, as near as possible, the same spot. It is also worth noting that the SWCNT growth area occupied only a small part of the sample surface, and enhancement of the emission signal was only observed when the laser beam was directed at a portion of the sample known to contain SWCNTs.

The first two spectra recorded at 300 K and 380 K have been scaled up $500x=1/0.002$ to facilitate visual comparison, and all data have been scaled appropriately to approximately account for effects of the analyzer's settings (electron pass energy E_{pass} and the analyzer's slit setting), which were necessarily adjusted during the course of the experiments. Strikingly, cooling the sample from 570 K to room temperature caused the laser-enhanced EEDs (green crosses) to shift approximately 0.25 eV to higher energies (larger effective work function ϕ) and to decrease dramatically in magnitude. Thereafter, as the sample was reheated to 570 K, the effective work function decreased to nearly its originally measured value of 1.96 eV. Cooling the sample again to room temperature and reheating it to 570 K verified that the temperature dependence of measured EEDs was repeatable and that an effective work function of approximately 2 eV was recovered each time the sample was reheated to 570 K. Similar behavior has also been observed in other samples, as the temperature was cycled between 300 and 570 K multiple times, resulting in a shift of the effective work function that is not completely reversible but increases slightly after each thermal cycle presumably due to the loss of some K atoms.

Subsequent heating of the sample above 570 K caused the laser-assisted emission peak to shift to higher energies and to decrease in magnitude. At 700 K, pure thermionic emission (laser shuttered, shown by black dots) became significant although the shape of its distribution is not visible in Fig. 8(a) because of its relatively small magnitude. In Fig. 8(b) the EEDs have been normalized to better compare their shapes and magnitudes, and theoretical curve fits based on Eq. (1) are also included. EEDs collected at temperatures below 700 K and with the laser shuttered are not shown in Fig. 8(b) because they are dominated by background noise. Importantly, the thermionic and laser-assisted EEDs collected at 700 K are nearly identical in shape and position on the energy axis [Fig. 8(b)], although the magnitude of the thermionic EED recorded at 700 K is much less than that of the laser-assisted EED [see Fig. 8(a)]. Likewise, as the sample was heated above 700 K, the pure thermionic and laser-assisted EEDs shifted to higher energies together, and the magnitudes of the thermionic EEDs increased relative to those of the laser-assisted EEDs.

Unfortunately, interpreting EED data from potassium-intercalated carbon nanotubes is a complicated task, and the mechanism that causes the EEDs to shift with changing temperature is not understood at present, although the (changing) positions of potassium atoms within the CNT lattice are certainly a factor.[54] Laser heating of the substrate can be discounted as a small factor as demonstrated by at least three arguments. First, pure thermionic emission under dark conditions is not observable until the substrate is heated to 700 K, while laser-enhanced EEDs are readily observable at 300 K. Thus, laser heating would need to cause a temperature rise of more than 400 K for it to be significant, which is in contrast to the theoretical prediction of less than 2 K calculated in Sec. II. Second, laser illumination is not observed to enhance thermionic emission from samples with work functions greater than 2.7 eV, for which the photon energy is not sufficient to produce emission by direct photoexcitation.[9,37] Third, at the highest substrate temperature, for which the electron emission is clearly thermionic, laser illumination does not noticeably affect the measured EED, establishing again that laser heating must be a small effect.

The most likely cause of the observed temperature-dependent shifts of the EEDs is that the potassium atoms change position as temperature increases. It is well established that potassium atoms become highly mobile in the CNT lattice as the temperature increases above 300 K.[54,55] In the range of 300–570 K, the effective sample work function ϕ may decrease with increasing temperature because intercalated potassium atoms are more able to occupy critical locations on the sample surface. However, as temperature increases above 570 K, the intercalated potassium atoms become increasingly unstable and prone to desorption, resulting in a larger effective work function of the sample. Another important observation is that the thermionic and laser-

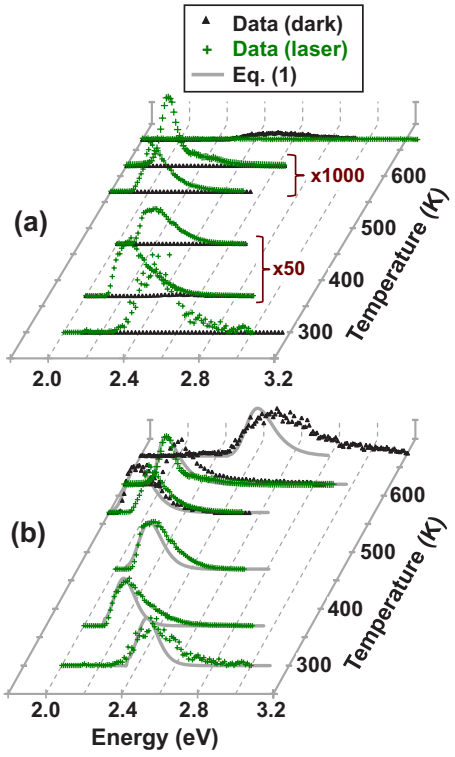

FIG. 9. (Color online) Thermionic and laser-assisted EEDs from a potassium-intercalated multiwalled CNT (K/MWCNT) sample. In (a) the EED magnitudes have been adjusted to account for the energy analyzer's settings and in (b) the EEDs have been normalized and theoretical fits included based on Eq. (1). Data in (a) dominated by background noise are not shown in (b): $V_{accel}=-4.5$ V.

assisted EEDs exhibit similar shapes in contrast to predictions of photoemission theory as illustrated in Fig. 1, an indication that a substantial number of photoexcited electrons thermalize (i.e., undergo one or more scattering events) before finally ejecting from the sample. It is this observation that the majority of photoexcited electrons are scattered and become thermalized before ultimately emitting from the sample that has motivated us to use thermionic theory [Eq. (1)] rather than photoemission theory [Eq. (4)] for the curve fits in Fig. 8(b).

E. K/MWCNT sample

Several samples consisting of random arrays of multiwalled carbon nanotubes were also subjected to the intercalation process described above, and electron emission energy distributions collected from an individual sample are shown in Fig. 9. The EEDs were recorded under conditions similar to those of the single-walled CNT sample featured in Figs. 7 and 8, except that the laser was focused to a spot size of 0.2 mm resulting in an intensity of approximately 370 W/cm^2, which is still expected to cause negligible heating. Similar to the previous results, the EEDs of Fig. 9 have also been scaled to account for effects of the analyzer's settings. In addition, the EEDs collected at 370 and 470 K have been scaled down 50x to facilitate visual comparison. Similarly, the EEDs collected at 570 and 620 K have been scaled down 1000x. All data in Fig. 9 were obtained with the laser illuminating as near as possible the same point on the sample surface although substantial emission could be obtained with the laser illuminating almost any part of the sample, which was nearly entirely covered with MWCNTs.

The smallest effective sample work function, approximately 1.9 eV, was observed at 570 K and cooling the sample to room temperature caused the work function to increase to approximately 2.4 eV. As with other samples, the MWCNT sample featured in Fig. 9 was heated to 570 K and cooled to room temperature multiple times, and the work function was observed to decrease and increase nearly reversibly with each temperature cycle. For clarity, electron emission energy distributions from only a single heating sequence are shown in Fig. 9. After heating the sample briefly to 670 K [uppermost curves in Figs. 9(a) and 9(b)], the sample was cooled to room temperature and loaded in a different vacuum system for XPS characterization, the results of which have been shown in Fig. 4. Notably, the agreement between the shapes and positions of the high-temperature thermionic EEDs and the laser-assisted EEDs is not as good in Fig. 9 as for the single-walled CNT sample featured in Fig. 8; however, the pure thermionic and laser-assisted EEDs still appear highly correlated.

Although the low work function values achieved by K-intercalated CNT samples is promising, the total emitted electron current is very low, and future work will need to address this issue before practical applications can be developed. To illustrate this issue, we measured the total emission current of the K/MWCNT sample featured in Fig. 9 by connecting a Keithley 8486 picoammeter to the moveable stainless steel plate located above the sample in the vacuum chamber (see Fig. 5). At 570 K, a total emission current of 0.13 nA was collected from the steel bar with the laser illuminating the sample, and the measured emission current was independent of a voltage applied to the bar for the range of voltages tested (0–2 V, limited by the dc offset that could be applied to the picoammeter). Shuttering the laser beam immediately caused the recorded emission current to drop to approximately 0.002 nA. Similarly, moving the steel bar to a location further from the sample caused the emission current to decrease to approximately 0.003 nA, even with the laser beam illuminating the sample. Similar tests conducted at a sample temperature of 620 K revealed that the photoemission current increased to 0.19 nA with a background noise (laser shuttered) of approximately 0.005 nA. Thus, we conclude that emission currents of the K-intercalated CNT samples examined in this work are very small, indicating that the quantum emission efficiency (ratio of the number of emitted electrons to the number of incident photons) is also very low. The fact that the quantum emission efficiency is low is further evidence that the majority of photoexcited electrons are scattered and become partially thermalized before emitting from the sample.

IV. CONCLUSIONS

In this work, single- and multiwalled carbon nanotube arrays have been intercalated with potassium to reduce their

work functions from 4.5 eV to approximately 2 eV. Notably, electron emission results obtained over a wide temperature range from K-intercalated single-walled and multiwalled CNTs are strikingly similar although the samples are produced on very different substrates using different growth conditions. Control samples without CNTs were also subjected to the same intercalation procedure but did not exhibit significant emission for temperatures below 600 K. Potassium intercalation of a multiwalled CNT sample was confirmed using XPS characterization. Electron EEDs obtained using a hemispherical electron energy analyzer reveal that the effective work function of emitters prepared in this way is temperature-dependent and has a minimum of approximately 2 eV in the neighborhood of 570 K. Illumination of potassium-intercalated CNTs with a 532 nm, 100 mW laser resulted in EEDs that closely match thermionic emission theory but with substantially greater magnitudes, potentially indicating that a large fraction of photoexcited electrons partially thermalize (i.e., undergo one or more scattering events) before escaping from the sample. The conjecture that many photoexcited electrons experience substantial scattering before eventual emission is further supported by the fact that very low emission currents (nanoamperes) were observed to result from relatively large levels of laser power (milliwatts). Much larger quantum emission efficiencies (ratio of the number of emitted electrons to the number of incident photons) are needed for practical applications, such as for free electron lasers or photoenhanced thermionic emission power generators.

ACKNOWLEDGMENTS

The authors wish to thank the National Science Foundation's Nanoscale Science and Engineering program under Award No. CTS-0210366 for assistance in funding this project.

APPENDIX: DILOGARITHM FUNCTION EVALUATION

The dilogarithm function is not commonly used and is defined here for the reader's convenience,[22]

$$\mathrm{dilog}(x) = \int_1^x \frac{\ln(t)}{1-t}dt. \tag{A1}$$

For computational purposes, the dilogarithm function can be calculated efficiently as a series[22,23]

$$\mathrm{dilog}(x) = \begin{cases} \displaystyle\sum_{k=1}^{\infty} \frac{(1-x)^k}{k^2}, & 0 \le x \le 2 \\ \displaystyle -\frac{\pi^2}{6} - \frac{1}{2}\ln(x-1)^2 - \sum_{k=1}^{\infty}\left(\frac{-1}{x-1}\right)^k \frac{1}{k^2}, & x > 2. \end{cases} \tag{A2}$$

We note that for practical values of the argument x, the infinite series in Eq. (A2) is well approximated using only the first few terms.

[1]H. Ago, T. Kugler, F. Cacialli, W. R. Salaneck, M. S. P. Shaffer, A. H. Windle, and R. H. Friend, J. Phys. Chem. B **103**, 8116 (1999).
[2]J. P. Sun, Z. X. Zhang, S. M. Hou, G. M. Zhang, Z. N. Gu, X. Y. Zhao, W. M. Liu, and Z. Q. Xue, Appl. Phys. A: Mater. Sci. Process. **75**, 479 (2002).
[3]P. Liu, Y. Wei, K. Jiang, Q. Sun, X. Zhang, S. Fan, S. Zhang, C. Ning, and J. Deng, Phys. Rev. B **73**, 235412 (2006).
[4]S. Suzuki, C. Bower, Y. Watanabe, and O. Zhou, Appl. Phys. Lett. **76**, 4007 (2000).
[5]S. Suzuki, F. Maeda, Y. Watanabe, and T. Ogino, Phys. Rev. B **67**, 115418 (2003).
[6]V. S. Robinson, T. S. Fisher, J. A. Michel, and C. M. Lukehart, Appl. Phys. Lett. **87**, 061501 (2005).
[7]X. H. Qiu, M. Freitag, V. Perebeinos, and P. Avouris, Nano Lett. **5**, 749 (2005).
[8]G. Y. Slepyan, M. V. Shuba, S. A. Maksimenko, and A. Lakhtakia, Phys. Rev. B **73**, 195416 (2006).
[9]T. L. Westover, Ph.D. thesis, Purdue University, 2008.
[10]K. Uppireddi, T. L. Westover, T. S. Fisher, B. R. Weiner, and G. Morell, J. Appl. Phys. **106**, 043716 (2009).
[11]V. S. Robinson, Y. Show, G. M. Swain, R. G. Reifenberger, and T. S. Fisher, Diamond Relat. Mater. **15**, 1601 (2006).
[12]G. N. Hatsopoulos and E. P. Gyftopoulos, *Thermionic Energy Conversion* (MIT Press, Cambridge, MA, 1973).
[13]R. T. Ross, J. Appl. Phys. **54**, 2883 (1983).
[14]C. Hernandez-Garcia, P. G. O'Shea, and M. L. Stutzman, Phys. Today **61**(2), 44 (2008).
[15]E. Sabia, G. Dattoli, A. Dipace, and G. Messina, Phys. Plasmas **15**, 033104 (2008).
[16]K. L. Jensen, N. A. Moody, D. W. Feldman, E. J. Montgomery, and P. G. O'Shea, J. Appl. Phys. **102**, 074902 (2007).
[17]R. Ganter, R. J. Bakker, C. Grough, M. Paraliev, M. Pedrozzi, F. Le Pimpec, L. Rivkin, and A. Wrulich, Nucl. Instrum. Methods Phys. Res. A **565**, 423 (2006).
[18]T. Rao *et al.*, Nucl. Instrum. Methods Phys. Res. A **557**, 124 (2006).
[19]K. L. Jensen, D. W. Feldman, and P. G. O'Shea, Phys. Rev. ST Accel. Beams **6**, 083501 (2003).
[20]R. D. Young, Phys. Rev. **113**, 110 (1959).
[21]J. W. Gadzuk and E. W. Plummer, Rev. Mod. Phys. **45**, 487 (1973).
[22]I. A. Stegun, in *Handbook of Mathematical Function*, edited by M. Abramowitz and I. A. Stegun (Dover, New York, NY, 1972), p. 1004.
[23]H. B. Dwight, *Tables of Integrals and Other Mathematical Data* (Macmillan, New York, NY, 1961), pp. 144 and 242.
[24]A. C. Marshall, Surf. Sci. **517**, 186 (2002).
[25]F. A. M. Köck, J. M. Garguilo, B. Brown, and R. J. Nemanich, Diamond Relat. Mater. **11**, 774 (2002).
[26]R. G. Forbes, Solid-State Electron. **45**, 779 (2001).
[27]*Photoemission in Solids I*, edited by M. Cardona and L. Ley (Springer-Verlag, New York, NY, 1978).
[28]*Photoemission and the Electronic Properties of Surfaces*, edited by B. Feuerbacher, B. Fitton, and R. F. Willis (Wiley, New York, NY, 1978).
[29]R. H. Fowler, Phys. Rev. **38**, 45 (1931).
[30]L. A. DuBridge, Phys. Rev. **43**, 727 (1933).
[31]N. A. Papadogiannis, S. D. Moustaïzis, and J. P. Girardeau-Montaut, J. Phys. D **30**, 2389 (1997).
[32]J. H. Bechtel, W. L. Smith, and N. Bloembergen, Phys. Rev. B **15**, 4557 (1977).
[33]In order to simplify the evaluation of the integral in Eq. (5), it has also been assumed that the photon energy $\hbar\omega$ is greater than the emitter's Fermi level (measured from the bottom of the conduction band) so that all electrons in the conduction band can become photoexcited.
[34]P. A. Tipler and R. A. Llewellyn, *Modern Physics*, 3rd ed. (Freeman, New York, NY, 1999).
[35]S. Mogren and R. Reifenberger, Surf. Sci. **186**, 232 (1987).
[36]W. E. Spicer, Phys. Rev. **125**, 1297 (1962).
[37]Using different techniques, many samples have been prepared with work functions ranging from 2.5 to 4.5 eV (see Ref. 9), and for all of these samples, raising the temperature of the substrate heater by 20 K dramatically affects thermionic emission intensity. However, for samples with

work functions greater than 2.7 eV, in which the photoelectric effect is dormant, laser illumination does not noticeably affect the thermionic emission intensity. Therefore, laser heating at the sample extremity must be less than 20 K.
[38]H. S. Carslaw and J. C. Jaeger, *Conduction of Heat in Solids* (Oxford University Press, New York, NY, 1986).
[39]R. D. Young and C. E. Kuyatt, Rev. Sci. Instrum. **39**, 1477 (1968).
[40]R. Reifenberger, H. A. Goldberg, and M. J. G. Lee, Surf. Sci. **83**, 599 (1979).
[41]K. Wandelt, Appl. Surf. Sci. **111**, 1 (1997).
[42]J. R. Smith, G. L. Bilbro, and R. J. Nemanich, Phys. Rev. B **76**, 245327 (2007).
[43]M. R. Maschmann, A. D. Franklin, A. Scott, D. B. Janes, T. S. Fisher, and T. D. Sands, Nano Lett. **6**, 2712 (2006).
[44]A. D. Franklin, M. R. Maschmann, M. DaSilva, D. B. Janes, T. D. Sands, and T. S. Fisher, J. Vac. Sci. Technol. B **25**, 343 (2007).
[45]A. D. Franklin, J. T. Smith, T. D. Sands, T. S. Fisher, K.-S. Choi, and D. B. Janes, J. Phys. Chem. C **111**, 13756 (2007).
[46]S. Ujereh, T. S. Fisher, and I. Mudawar, ASME Trans. J. Heat Transfer **50**, 4023 (2007).
[47]J. A. Michel, V. S. Robinson, S. L. Yang, S. Sambandam, W. Lu, T. Westover, T. S. Fisher, C. M. Lukehart, J. Nanosci. Nanotechnol. **8**, 1942 (2008).
[48]S. Suzuki and M. Tomita, J. Appl. Phys. **79**, 3739 (1996).
[49]J. Li, V. S. Robinson, Y. Liu, W.u, T. S. Fisher, and C. M. Lukehart, Nanotechnology **18**, 325606 (2007).
[50]S. Li, E. T. Kang, K. G. Neoh, Z. H. Ma, K. L. Tan, and W. Huang, Appl. Surf. Sci. **181**, 201 (2001).
[51]J. F. Moulder, W. F. Stickle, P. E. Sobol, and K. D. Bombden, *Handbook of X Ray Photoelectron Spectroscopy* (Physical Electronics, Eden Prairei, MN, 1995).
[52]B. Lamontagne, F. Semond, and D. Roy, J. Electron Spectrosc. Relat. Phenom. **73**, 81 (1995).
[53]Specs Phoibos Hemispherical Energy Analyzer User Manual, Order No. 78 000 101.
[54]L. Grigorian, G. U. Sumanasekera, A. L. Loper, S. Fang, J. L. Allen, and P. C. Eklund, Phys. Rev. B **58**, R4195 (1998).
[55]M. Radosavljević, J. Appenzeller, and Ph. Avouris, Appl. Phys. Lett. **84**, 3693 (2004).